Interfacial precipitation of the M_5B_3-type boride in Ni-based superalloys

X. B. Hu, L. Z. Zhou, J. S. Hou, X. Z. Qin & X. L. Ma

Published online: 28 Jun 2016.

Submit your article to this journal ↗

View related articles ↗

View Crossmark data ↗

Taylor & Francis
Taylor & Francis Group

Interfacial precipitation of the M_5B_3-type boride in Ni-based superalloys

X. B. Hu[a,1], L. Z. Zhou[b], J. S. Hou[b], X. Z. Qin[b] and X. L. Ma[a]

[a]Shenyang National Laboratory for Materials Science, Institute of Metal Research, Chinese Academy of Sciences, Shenyang, China; [b]Superalloys Division, Institute of Metal Research, Chinese Academy of Sciences, Shenyang, China

ABSTRACT

Microstructural characteristics of an experimental Ni-based superalloy with boron addition subjected to a long-term ageing treatment were systematically investigated by various kinds of transmission electron microscopy technique. Based on detailed electron diffraction analyses, we found that there are many nanosized M_5B_3 precipitates in our long-term ageing alloys, which keeps a good orientation relationship with the γ/γ' matrix. Furthermore, the precipitation characteristics of M_5B_3 phase were clarified. It is found that the M_5B_3-type boride prefers to precipitate at the γ/γ' interfaces and low-angle grain boundaries. These interfacial nanosized precipitates can play the role of pinning effect and are expected to be advantageous for postponing the γ' rafting and low-angle grain boundary migration to some extent at high temperature.

1. Introduction

On account of their superior creep and corrosion-resistant properties at high temperature, Ni-based superalloys are widely utilized in the hot section of aircraft engines and land-based gas turbines [1]. Among many failure modes of high temperature materials, creep is an important one. Though the grain boundary strengthening effect is very remarkable at room temperature, the role of grain boundaries is totally adverse for the high-temperature creep property of superalloys because of their migration during creep process. And unfortunately, there are many grain boundaries in conventional cast superalloys. Even for the single crystal superalloys, a large number of low-angle grain boundaries still exist. Thus, for strengthening the grain boundaries at high temperature, microelements carbon and boron are widely added into superalloys [2–4]. Therefore, besides existence in the austenitic solid solution form, precipitations of carbide and boride in superalloys are always inevitable [5–10]. Thus, a systematic knowledge towards the microstructural features of carbide/boride is very crucial for a better understanding of the structure related mechanical phenomena. Furthermore, with the extension of service time at high temperature, the microstructures

of materials tend to deviate greatly from their pristine state. Meanwhile, considering the extremely aggressive service environment, the performance of critical components is especially sensitive to the microstructures of materials. Therefore, microstructural assessment of the experimental alloys subjected to a long-term ageing treatment is always necessary.

In contrast to carbide, available reports on boride precipitated in superalloys are very limited. Generally speaking, there are mainly three types of boride in superalloys, namely the M_3B_2-, M_5B_3- and M_2B-type boride, where M represents the transition metal atoms [8,11–14]. Though above three types of boride precipitated in our long-term ageing alloys, in the present work, we only focus on the M_5B_3-type boride. The precipitation of M_5B_3-type boride was first recognized by Zhang in IN738 [6], where its effect on the grain boundary liquation temperature during the weld heat-affected zone thermal cycle was briefly discussed. Later on, Zhang found that M_5B_3 phase also precipitated in Rene 80 when exposed at 1025 °C for 6 h. Furthermore, the precipitates also maintain a good orientation relationship with the matrix [7]. However, the detailed precipitation characteristic of this phase, which is significant for a comprehensive assessment of its effect on mechanical properties, is still lacking up to now. Therefore, by means of various kinds of TEM technique, we expect to clarify more detailed microstructural characteristics of the M_5B_3 phase precipitated in our alloys.

2. Experimental procedure

The used alloy in the present work is a high-temperature corrosion-resistant Ni-based superalloy with the nominal chemical composition of 15.5 Cr, 10.8 Co, 2.1 Mo, 5.6 W, 3.2 Al, 4.6 Ti, 0.2 Nb, 0.4 Hf, 0.073 C, 0.075 B, and balance Ni, in wt %. After the standard heat treatment, the experimental superalloy was exposed at 900 °C for 10,000 h and then air-cooled. For transmission electron microscopy (TEM) imaging, electron transparent foils were prepared by cutting, grinding and dimpling the materials to a thickness less than 10 μm in the central area with a diameter of 3 mm. The final thinning was performed by Ar ion milling in a Gatan precision ion polishing system. Before loading into the TEM, the thin foils were cleaned by the Fischione plasma cleaner for removing the surface contamination.

Electron diffraction analyses were performed on JEM-2100 operated at 200 kV. HAADF-STEM images and the localized composition analysis were conducted on Tecnai G^2 F30, which was equipped with a high-angle annular dark field (HAADF) detector, X-ray energy-dispersive spectrometer (EDS) systems and Gatan imaging filter (GIF) system and operated at 300 kV. The energy filter TEM (EFTEM) images were recorded by the three-window method and the slit width used here was 20 eV.

3. Results and discussion

Figure 1a HAADF image displays a typical microstructural characteristic in the experimental alloy subjected to a long-term ageing treatment with γ and γ′ phase indicated. Since the HAADF imaging technique provides a contrast which is approximately proportional to the square of atomic number (Z) [15–17], the γ phase shows a brighter contrast in contrast to γ′ indicating the higher average atomic number Z for γ phase. Compared with γ/γ′ matrix, the interfacial precipitates show the highest contrast, which means that the precipitates possess a higher average atomic number Z than γ phase. EDS result displayed in Figure 1b reveals that the precipitates are mainly composed of Cr, W, Mo and minor Ni. For an accurate
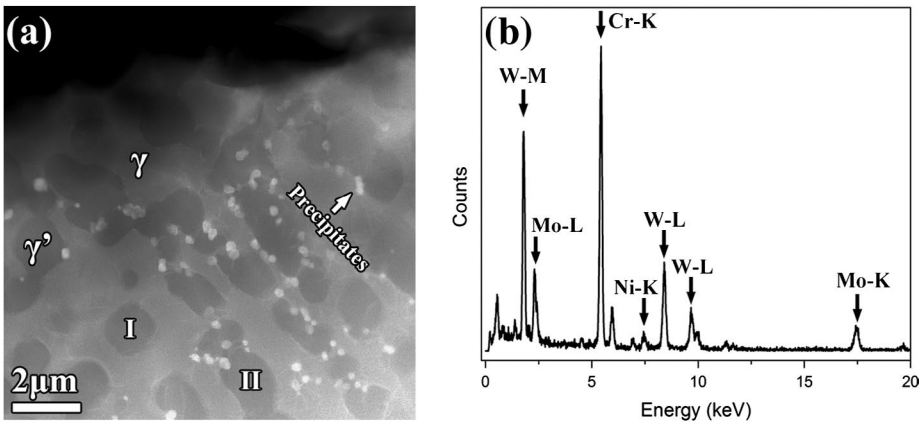
Figure 1. (a) HAADF image displaying the precipitation of M_5B_3 phase at the γ/γ' interface. The γ and γ' phases are indicated. The γ' labelled by I and II represent the relative regular and heavily rafted γ'. (b) EDS of the precipitates in (a).
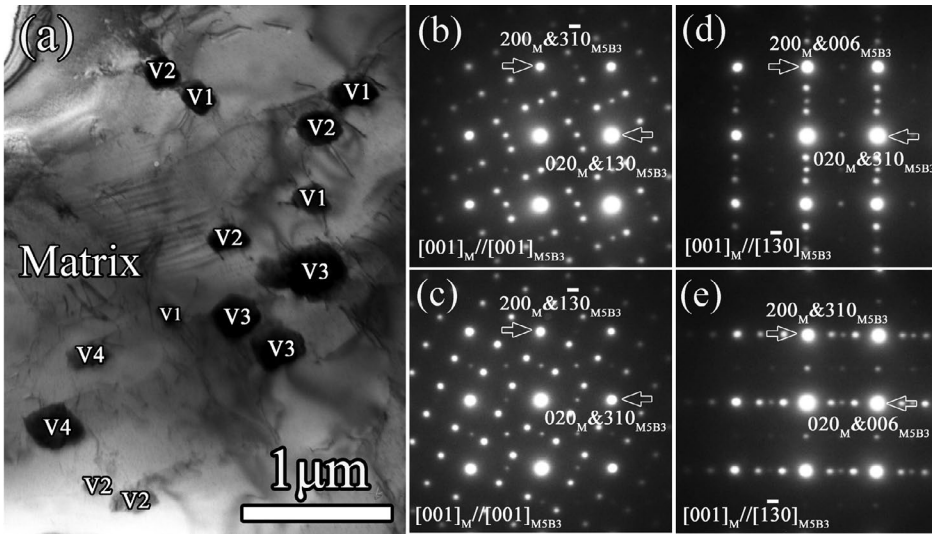

Figure 2. (a) BF image of the γ/γ' matrix and M_5B_3 precipitates. The V1-V4 indicates four types of orientation variants for M_5B_3 phase. Composite EDPs along (b) $[0\,0\,1]_M$ // $[0\,0\,1]_{M5B3}$ obtained from matrix and V1, (c) $[0\,0\,1]_M$ // $[0\,0\,1]_{M5B3}$ obtained from matrix and V2, (d) $[0\,0\,1]_M$ // $[1\,\bar{3}\,0]_{M5B3}$ obtained from matrix and V3, (e) $[0\,0\,1]_M$ // $[1\,\bar{3}\,0]_{M5B3}$ obtained from matrix and V4. The subscript M represents the matrix, including γ and γ' phase.

structural determination of these precipitates, detailed selected area electron diffraction (SAED) analyses were performed.

Figure 2a bright field (BF) image displays the region used for SAED analyses. Based on the composite electron diffraction patterns (EDPs) shown in Figure 2b–e, which are obtained from the regions including both matrix and precipitates, it is found that the precipitates keep a good orientation relationship (OR) with the γ/γ' matrix. Reflections from the γ/γ' matrix in Figure 2b–e can be indexed as $[0\,0\,1]_M$ zone-axis, where the subscript M represents the

γ/γ' matrix. And the precipitates can be determined as the M_5B_3 phase with the space group of I4/mcm and lattice parameters of a = 5.7 Å, c = 10.7 Å. But, interestingly, reflections from the M_5B_3 precipitates possess different distribution forms. Considering the lattice symmetry difference between M_5B_3 phase (tetragonal lattice) and matrix (cubic lattice), these M_5B_3 phase possessed different diffraction characteristics can actually be treated as different orientation variants as indicated in Figure 2a. As shown in Figure 2b, composite EDPs, the exact orientation relationship (OR) between matrix and M_5B_3 phase can be labelled as $[0\,0\,1]_M$ // $[0\,0\,1]_{M5B3}$ with $(2\,0\,0)_M$ // $(3\,\bar{1}\,0)_{M5B3}$, $(0\,2\,0)_M$ // $(1\,3\,0)_{M5B3}$. Though in Figure 2c, composite EDPs, the M_5B_3 phase can also be labelled as $[0\,0\,1]_{M5B3}$ zone-axis, distribution of the reflections from M_5B_3 phase has a 53° rotation along $[0\,0\,1]_{M5B3}$ in contrast to Figure 2b. Taking account of the fact that $(1\,3\,0)_{M5B3}$ and $(3\,1\,0)_{M5B3}$ planes are actually equivalent, this is understandable since a 53° rotation along $[0\,0\,1]_{M5B3}$ will make $(3\,1\,0)_{M5B3}$ plane overlap with $(0\,2\,0)_M$ plane. Similarly, on account of the equivalence among $[1\,0\,0]_M$, $[0\,1\,0]_M$ and $[0\,0\,1]_M$ directions in the cubic lattice, we can easily arrive at the following orientation variants as shown in Figure 2d and e. For displaying the OR between M_5B_3 phase and matrix more clearly, we introduce the matrix form, which is particularly helpful when any plane/direction from matrix is transformed to M_5B_3 boride. Taking orientation variant 1 (V1) with composite EDPs shown in Figure 2b for example, the relationship between the planes (hkl) and the directions [uvw] in the two phases can be written as:

$$(hkl)_{M5B3}// M (hkl)_M (hkl)_M// M^{-1}(hkl)_{M5B3}$$

$$[uvw]_M// M^t[uvw]_{M5B3}[uvw]_{M5B3}// \left(M^t\right)^{-1}[uvw]_M.$$

The M here represents a basic matrix which transforms a plane in matrix to M_5B_3 boride. The M^t and M^{-1} represent the transposed and inverse matrix of M respectively. If we take into account the parallelism between the directions mentioned previously, we obtain the following matrix M:

$$M = \frac{1}{2}\begin{pmatrix} 3 & 1 & 0 \\ -1 & 3 & 0 \\ 0 & 0 & 6 \end{pmatrix}$$

Besides precipitation at the γ/γ' interface, it is found that M_5B_3 phases also tend to precipitate along the grain boundary as shown in Figure 3a. The inset Kikuchi patterns correspond to matrix grain I and II. When grain I is orientated along the exact $[0\,0\,1]_M$ zone-axis, gain II is slightly deviated from the exact $[0\,0\,1]_M$ direction for about 2°. In other words, Figure 3a shows a low-angle grain boundary. During our experimental process, the phenomenon of precipitation at low-angle grain boundaries is reproducible. In addition, M_5B_3 boride precipitated along the low-angle grain boundaries also keeps a good OR with one of the grains. Figure 3b and c are composite EDPs obtained from the regions around the grain boundaries. Figure 3b composite EDPs correspond to the region included matrix, and variants 1, 2 and 3, which can be produced by overlapping the EDPs of Figure 2b–d. While, Figure 3b composite EDPs correspond to the region included matrix, and variants 1, 2, 3 and 4, which can be produced by overlapping the EDPs of Figure 2b–e.
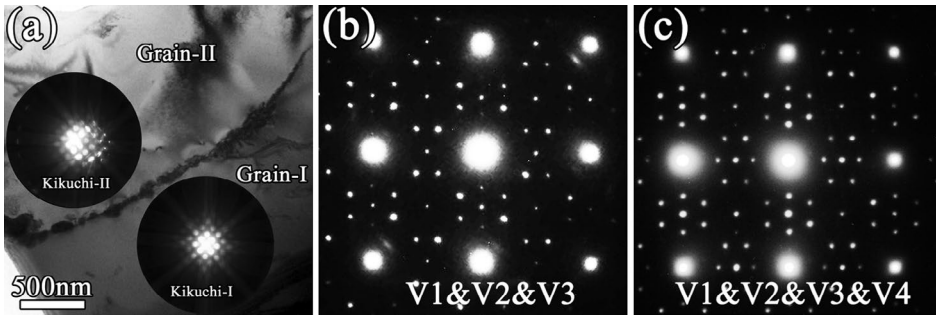
Figure 3 BF image displaying the precipitation of M_5B_3 phase along the low-angle grain boundary. Inset shows the Kikuchi pattern of the corresponding matrix grain. Composite EDPs included matrix and (a) V1, V2, V3 and (b) V1, V2, V3, V4.
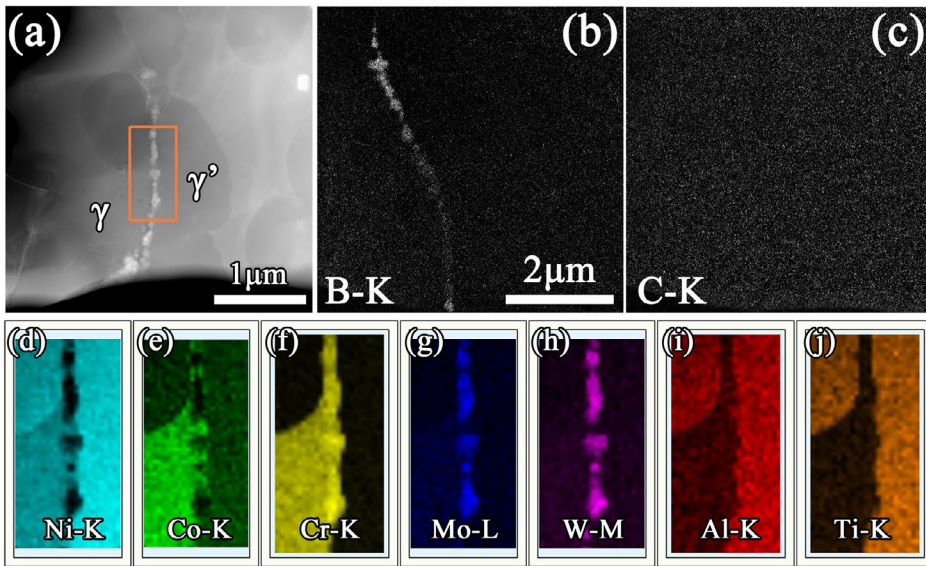

Figure 4. (a) HAADF image displaying the grain boundary precipitation. The rectangle frame indicated the EDS mapping region. Energy filter transmission electron microscopy (EFTEM) image of the element (b) boron and (c) carbon corresponding to the same region. EDS map imaged by (d) Ni-K, (e) Co-K, (f) Cr-K, (g) Mo-L, (h) W-M, (i) Al-K and (j) Ti-K.

In order to display more detailed relative compositional distribution, microanalyses were further performed on the low-angle grain boundary as shown in Figure 4a–j. Figure 4a HAADF image displays the phenomenon of precipitation along the low-angle grain boundary, where γ, γ' phase and the frame region used for EDS mapping are indicated. Figure 4d–j EDS maps are imaged by Ni-K, Co-K, Cr-K, Mo-L, W-M, Al-K and Ti-K, respectively. Compared with the γ/γ' matrix, it is found that M_5B_3 precipitates are richer in W, Mo and Cr, and more lack in Ni. On account of the intrinsic limitation of EDS in detecting light elements, the energy filter TEM based on the electron energy loss spectrometry (EELS) technique were utilized to reveal the distribution of light elements, boron and carbon since possibly there is carbon solution in the boride [18]. Interestingly, as shown in Figure 4b and

c EFTEM image, imaged by B-K and C-K, respectively, it is found that there is no detectable C signal along the low-angle grain boundary though the contents of C and B in our alloy are almost the same. In other words, precipitates along the low-angle grain boundaries in the present alloys are indeed boride but not carbo-boride.

Generally speaking, during our extensive TEM observations for samples subjected to the long-term ageing treatment, the above interfacial precipitation of M_5B_3-type boride was very common. And the grain size of M_5B_3 boride ranges from 200 to 500 nm. As for the precipitates at γ/γ' interface shown in Figure 1a, compared with the I-type γ', which is not obviously rafted, the M_5B_3 phases tend to precipitate at the interface between the rafted γ' and γ phase. Therefore, it is deduced that M_5B_3 precipitates possibly formed during the rafting process accompanying the redistribution of various chemical elements. And once formed, these nanosized precipitates are expected to play the role of pinning effect, which can hind the migration of the γ/γ' interface. Similarly, at high temperature, elemental redistribution also occurs at the grain boundaries. Once the nanosized M_5B_3 phase precipitated along the grain boundaries, these nanosized precipitates can also restrain the grain boundaries migration to some extent. Thus, the above interfacial precipitation phenomena are beneficial for improving the high-temperature creep strength of superalloys. In addition, the interfacial precipitation of M_5B_3 phase is also expected to appear in other types of superalloys with B addition. Furthermore, we would like to point out here that the precipitation of nanosized precipitates at γ/γ' interface and low-angle grain boundaries is only found for the M_5B_3 phase in our alloys. While the carbide and other types of borides tend to precipitate in grain interior and along the random grain boundaries. This is possibly related with the low interfacial energy between M_5B_3 phase and matrix. The exact reasons for above interfacial precipitation behaviour are beyond the scope of this present work but are still necessary to be further evaluated.

4. Conclusion

In summary, we presented a detailed microstructural investigation on the nanosized M_5B_3-type boride precipitated in a long-term ageing Ni-based superalloy. The orientation relationship between M_5B_3 phase and the γ/γ' matrix can be best stated as $[0\,0\,1]_M//[0\,0\,1]_{M5B3}$, $(2\,0\,0)_M // (3\,\bar{1}\,0)_{M5B3}$. Because of the lattice symmetry difference between M_5B_3 phase and matrix, there are four distinguishable M_5B_3 variants in the matrix. In addition, M_5B_3 phase tends to precipitate at the γ/γ' interfaces and low-angle grain boundaries. Considering the good OR between M_5B_3 phase and matrix and the related precipitation characteristics of M_5B_3, we suppose that these nanosized precipitates should play a beneficial role during the creep process at high temperature.

Disclosure statement

No potential conflict of interest was reported by the authors.

Funding

References

[1] R.C. Reed (ed.), *The Superalloys: Fundamentals and Applications*, Cambridge University Press, Cambridge, 2006.
[2] L. Xiao, D.L. Chen and M.C. Chaturvedi, Metall. Mater. Trans. A 35 (2004) p.3477–3487.
[3] L. Xiao, D.L. Chen and M.C. Chaturvedi, Metall. Mater. Trans. A 36 (2005) p.2671–2684.
[4] L. Xiao, D.L. Chen and M.C. Chaturvedi, Metall. Mater. Trans. A 437 (2006) p.157–171.
[5] L.Z. He, Q. Zheng, X.F. Sun, H.R. Guan, Z.Q. Hu, A.K. Tieu, C. Lu and H.T. Zhu, Mater. Sci. Eng. A 397 (2005) p.297–304.
[6] H.R. Zhang, O.A. Ojo and M.C. Chaturvedi, Scr. Mater. 58 (2008) p.167–170.
[7] H.R. Zhang and O.A. Ojo, J. Mater. Sci. 43 (2008) p.6024–6028.
[8] H.R. Zhang and O.A. Ojo, Philos. Mag. 90 (2010) p.765–782.
[9] X.B. Hu, Y.B. Xue, S.J. Zheng, Y.L. Zhu, D. Chen and X.L. Ma, J. Alloys Compd. 611 (2014) p.104–110.
[10] X.B. Hu, Y.L. Zhu, L.Z. Zhou, B. Wu and X.L. Ma, Philos. Mag. Lett. 95 (2015) p.237–244.
[11] M.J. Kaufman and V.I. Levit, Philos. Mag. Lett. 88 (2008) p.259–267.
[12] X.B. Hu, Y.L. Zhu and X.L. Ma, Acta Mater. 68 (2014) p.70–81.
[13] X.B. Hu, Y.L. Zhu, N.C. Sheng and X.L. Ma, Sci. Rep. 4 (2014) p.7367.
[14] X.Z. Qin, J.T. Guo, C. Yuan, C.L. Chen and H.Q. Ye, Metall. Mater. Trans. A 38 (2007) p.3014–3022.
[15] S.J. Pennycook and D.E. Jesson, Phys. Rev. Lett. 64 (1990) p.938–941.
[16] S.J. Pennycook, Adv. Imag. Elect. Phys. 123 (2002) p.173–206.
[17] S.J. Pennycook, Ultramicroscopy 30 (1989) p.58–69.
[18] S. Ma, J. Xing, H. Fu, Y. Gao and J. Zhang, Acta Mater. 60 (2012) p.831–843.